Applied Catalysis B: Environmental 306 (2022) 121095

Contents lists available at ScienceDirect

Applied Catalysis B: Environmental

journal homepage: www.elsevier.com/locate/apcatb

Monodispersed ruthenium nanoparticles interfacially bonded with defective nitrogen-and-phosphorus-doped carbon nanosheets enable pH-universal hydrogen evolution reaction

Wenqiang Li [a,1], Heng Zhang [a,b,1], Ka Zhang [a,b], Wenxuan Hu [a], Zezhong Cheng [a], Haipeng Chen [a], Xun Feng [a,*], Tao Peng [c,*], Zongkui Kou [d,*]

[a] College of Chemistry and Chemical Engineering, Luoyang Normal University, Luoyang 471934, PR China
[b] College of Chemistry, Zhengzhou University, Zhengzhou 450001, PR China
[c] Department of Electrical and Computer Engineering, University of Toronto, Toronto, Ontario M5S 3G4, Canada
[d] State Key Laboratory of Advanced Technology for Materials Synthesis and Processing, Wuhan University of Technology, Wuhan 430070, China

ARTICLE INFO

Keywords:
Ruthenium
Electrocatalysts
Interfacial bond
Hydrogen evolution
DFT calculation

ABSTRACT

Herein, we significantly accelerated the kinetics of hydrogen evolution reaction (HER) by interfacially bonding ruthenium nanoparticles with defect-rich nitrogen and phosphorus co-doped carbon nanosheets (Ru/D-NPC). The optimal Ru/D-NPC therefore achieves ultralow overpotentials of 23, 61, and 68 mV at the current density of 10 mA cm^{-2} for HER in alkaline, neutral, and acidic electrolytes, respectively, demonstrating the excellent pH-universal HER activities. Specially, our Ru/D-NPC catalysts represent a 2 × advance in mass activity (639.9 mA/mg_{Ru}) compared to benchmarking Pt/C catalysts (320 mA/mg_{Pt}) and high per-site activity (0.13 s^{-1}) under alkaline conditions while remaining the excellent stability under all pH conditions. We experimentally demonstrated that Ru-N bonds at the interfaces of Ru/D-NPC strengthen the metal-support interaction and modulates the electronic structure of Ru, optimizing the intrinsic HER kinetics and sintering-resistance of active Ru species, as further rationalized by theoretical calculations. This work shines the light on the effect of interfacial bonds on the intrinsic HER kinetics.

1. Introduction

Hydrogen (H_2) has been consider as a promising clean energy carrier to replace fossil fuel due to its high energy density and harmless to environment [1,2]. At present, large-scale generation of high purity green hydrogen from cathodic hydrogen evolution reaction (HER) by water electrolysis is widely used method [3–5]. To date, platinum-based catalysts are the most advanced HER electrocatalysts in acidic solution in spite of their high cost and small reserves. However, their HER efficiency remains relatively low in alkaline and neutral electrolytes due to the slow reaction kinetics of additional water dissociation step [6,7]. In this regard, developing low-cost pH-universal HER catalysts with Pt-like activity and beyond is central to the field [8,9].

Ruthenium (Ru) is one of platinum group metals, with about 1/30 the price of Pt, representing a potential substitute to Pt for HER process [10,11]. In past few years, numerous efforts have been devoted to boosting HER kinetics on Ru-based electrocatalysts, typically by modulating the electronic structure and increasing the number of active Ru sites. For example, strong coupling Ru species on the optimal supporting material (e.g., conductive phosphides [12] and oxygen vacancy-enriched oxides [13], layered double hydroxides [14]) accelerate HER activity with good durability. However, there is still a considerable space for the performance improvement of Ru-based electrocatalysts, especially for HER in a wide pH range due to insufficient achievements.

Recently, coupling Ru with defective supportive materials offers an excellent strategy to improve the Ru activity and stability by metal-support interactions. Indeed, metal-support interactions accelerate charge transfer between metal and support and induce small clusters to increase the stability [15,16]. Profiting from the large surface area and uneven spin density after the introduction of heteroatoms, nitrogen and/or phosphorus doping of carbon (e.g., N-doped graphene) can be as

* Corresponding authors.
E-mail addresses: fengx@lynu.edu.cn (X. Feng), pengtao736@outlook.com (T. Peng), zongkuikou@whut.edu.cn (Z. Kou).
[1] These authors contributed equally.

https://doi.org/10.1016/j.apcatb.2022.121095
Received 15 November 2021; Received in revised form 24 December 2021; Accepted 9 January 2022
Available online 11 January 2022

an ideal supports [17–19]. NPC supported RuP_2 embedded shows Pt-like HER activity in all-pH range, as the interaction between RuP_2 and NPC optimizes the hydrogen adsorption energy and promises effective electron transfer in HER process [20]. In addition, surface defects in supports can supply small protective clusters to stabilize catalysts [21,22]. S doped defective C supported RuNi alloy exhibits the supper activity and durability due to the S-doped defective carbon as the support speeding up the charge transfer and protecting the inner alloy nanoparticles from electrolyte during the long-term electrochemical process [23]. Therefore, we focus this study on selecting suitable supports to enable strong interactions between the isolated Ru nanoparticles and the supports to achieve the required activity and stability of Ru-based catalysts at all pH for water splitting [22].

Herein, we sought therefore to engineer Ru catalysts interfacially bonded with nitrogen-and-phosphorus-doped carbon nanosheets (Ru/D-NPC) as a model to recognize the coordinative interaction between Ru and defect-rich carbon support to improve HER activity and stability. We reasoned that the N and P dopants in the carbon nanosheets can tune the charge distribution of C atoms and modulate the electron structure of Ru to enhance the HER activity and durability at various pH values. We therefore conduct X-ray photoelectron spectroscopy (XPS), electron spin resonance (ESR) spectrum, Raman spectra studies and density functional theory (DFT) calculations to rationalize the modulation of electronic structures, coordinative interaction of Ru and the mechanism of improved HER performance.

2. Experimental section

2.1. Materials and reagent

Melamine, P123, $Na_2WO_4{\cdot}2H_2O$, Ammonium phosphate monobasic ($NH_4H_2PO_4$), potassium hydroxide (KOH), $RuCl_3{\cdot}3H_2O$, sulfuric acid (H_2SO_4), absolute ethanol, and isopropyl alcohol were purchased from Sinopharm Chemical Reagent Co., Ltd. Commercial Pt/C (20 wt%), $RuCl_3{\cdot}3H_2O$, Iridium Dioxide (IrO_2) and Nafion (5 wt%) were obtained from Sigma-Aldrich. All the reagents are analytical grade and used without further treatment. Deionized (DI) water was employed as solvent.

2.2. Synthesis defective NPC nanosheets

To synthesis defective N and P doped C nanosheets, melamine (5 g), P123 (0.5 g), and $NH_4H_2PO_4$ (0.5 g) were dissolved in 50 mL water under vigorous stirring. After water shattered, the mixture of melamine-P123-$(NH_4)_2HPO_4$ can be obtained. Then the melamine-P123-$(NH_4)_2HPO_4$ dry gel and $Na_2WO_4{\cdot}2H_2O$ (0.33 g) were mixed in 50 mL water and dried at 80 °C for 12 h. The solids powders were transferred to a tubular furnace and heated at 300 °C for 1 h under Ar atmosphere first. Subsequently, the pyrolysis temperature was increased to 800 °C and kept for another 4 h. After cooling down to room temperature, the final WNPC products was obtained. To introduce defects in NPC, WNPC was immersed in 0.5 MH_2SO_4 for 8 h to etch W elements. After washing with deionized water and ethanol for three times, the defective NPC were obtained. Following the above method, the NPC, defective NC control sample were also prepared without the addition of $Na_2WO_4{\cdot}2H_2O$ and $NH_4H_2PO_4$, respectively.

2.3. Synthesis Ru/D-NPC

30 mg D-NPC was dispersed in 50 mL distilled water, and then 15 mL $RuCl_3.3\ H_2O$ solution (2 mg mL^{-1}) was added dropwise, followed by stirring at 70 °C overnight. The product was obtained by filtration, repeated washing with water and ethanol, followed by drying at 60 °C overnight. The synthesis methods of Ru/NPC and Ru/D-NC are the same as that of Ru/D-NPC, except that NPC and D-NC are used as the supports, respectively. The Ru/NPC and Ru/D-NC were prepared to elucidate the role of Ru and defect N in promoting HER process. The synthesis of Ru/D-NPC-1 and Ru/D-NPC-3 follows that of Ru/D-NPC, excepting that the amount of $RuCl_3.3\ H_2O$ is changed to 15 mg and 45 mg, respectively. The weight ratio of Ru in Ru/D-NPC-1 and Ru/D-NPC-3 is changed to optimize the HER performance. The material characterization, electrochemical measurements and theoretical calculation are detailed in Support Information.

3. Results and discussion

3.1. Structure of Ru/D-NPC

The Ru nanoparticles are uniformly prepared on nitrogen-and-phosphorus-doped carbon nanosheets (Ru/D-NPC) as illustrated in Fig. 1A. In detail, melamine, P123, $(NH_4)_2HPO_4$ and $Na_2WO_4{\cdot}2H_2O$ were mixed and then heated at high temperature of 800 °C to obtain W, N, P co-doped carbon (WNPC) nanosheets (Step I). Then, an acid treat process follows to etch W in the WNPC nanosheets and produce the defects and hierarchical pores (Step II). The obtained D-NPC nanosheets have therefore micro-meso-macropore structure, high N and P contents, enabling the physical confinement of Ru atoms on the D-NPC. Subsequently, Ru nanoparticles were deposited onto D-NPC nanosheets by a simple impregnation-adsorption method (Step III).

From the X-ray diffraction (XRD) results (Figure. S1), D-NPC shows a broad peak emerges at $2\theta = 26.1°$, due to graphitic C diffraction. Other three obvious diffraction peaks at $2\theta = 42.17°$, $44.01°$ and $69.5°$, correspond to (002), (101) and (110) plane of Ru (JCPDS No. 65–1863), respectively. N_2 adsorption-desorption isotherms (Figure. S2) indicate BET surface areas of 53.01, 60.78 and 79.67 $m^2\ g^{-1}$ for Ru/NPC, Ru/D-NC and Ru/D-NPC, respectively. We therefore conclude that Ru/D-NPC catalysts exhibit a slightly larger specific surface area and porous feature with the pore size around 4.45 nm.

The scanning electron microscopy (SEM) image of Ru/D-NPC (Fig. 1b) exhibits a three-dimensional cheese-like porous architecture with interconnected micropores. Such an interconnected hierarchical porous structure is potentially favorable for the mass transfer of reactants and electrolytes in the water splitting process, and facilitates the well dispersion and sinter-resistance of Ru throughout the entire supports [24,25]. The transmission electron microscopy (TEM) images show that ultrafine Ru nanocrystals are uniformly distributed on D-NPC (Fig. 1c) with an average diameter of 5.4 nm, which is ascribed to the multiscale confining effect of the defective D-NPC support [26]. From the High-resolution TEM (HRTEM) image (Fig. 1d), Ru nanoparticles were detected with a well-defined interplanar spacing of 0.217 nm, corresponds to the (002) facets of Ru [26]. The HAADF-STEM and corresponding elemental mapping (Fig. 1e–k) shows the homogeneous distributions of N, P, and Ru elements throughout the carbon nanosheets.

X-ray photoelectron spectroscopy (XPS) measurements were employed to identify the element states of Ru/D-NPC. The full XPS survey profiles (Fig. 2a) show the elements of C/Ru, N, P and O in Ru/D-NPC. The O elements are attributed to the surface oxide layer due to the exposition in the air during XPS experiments [27]. As displayed in Ru 3d+C 1 s in Ru/D-NPC (Fig. S3a), the peaks at 284.3, 285.6, and 287.8 eV correspond to C–C, C–N/C═N, and O-C═O, respectively [28]; while two spin–orbit peaks located at 281.2 and 285.2 eV, corresponding to the Ru $3d_{5/2}$ and Ru $3d_{3/2}$, confirming the metallic state of Ru [29]. The deconvoluted Ru 3p XPS spectrum for Ru/D-NPC (Fig. 2b) fitted at 462.9 and 485 eV correspond the metal Ru, while other two peaks at 465.2 and 487.7 eV correspond to the Ru $^{n+}$, probably due to chemical bonding of Ru with supports [30]. The P 2p spectrum is fitted with two sub-peaks (Fig. 2c), corresponding to P–C (131.9 eV) and P–O (133.3 eV), respectively [31]. The N 1 s spectrum of Ru/D-NPC is deconvoluted into four fitted peaks, corresponding to pyridinic N (398.2 eV), pyrrolic N (399.6 eV), and graphitic N (400.9 eV) and Oxidized N(402.5 eV) (Fig. 2d). Noting that, Ru 3p peaks of Ru/D-NPC

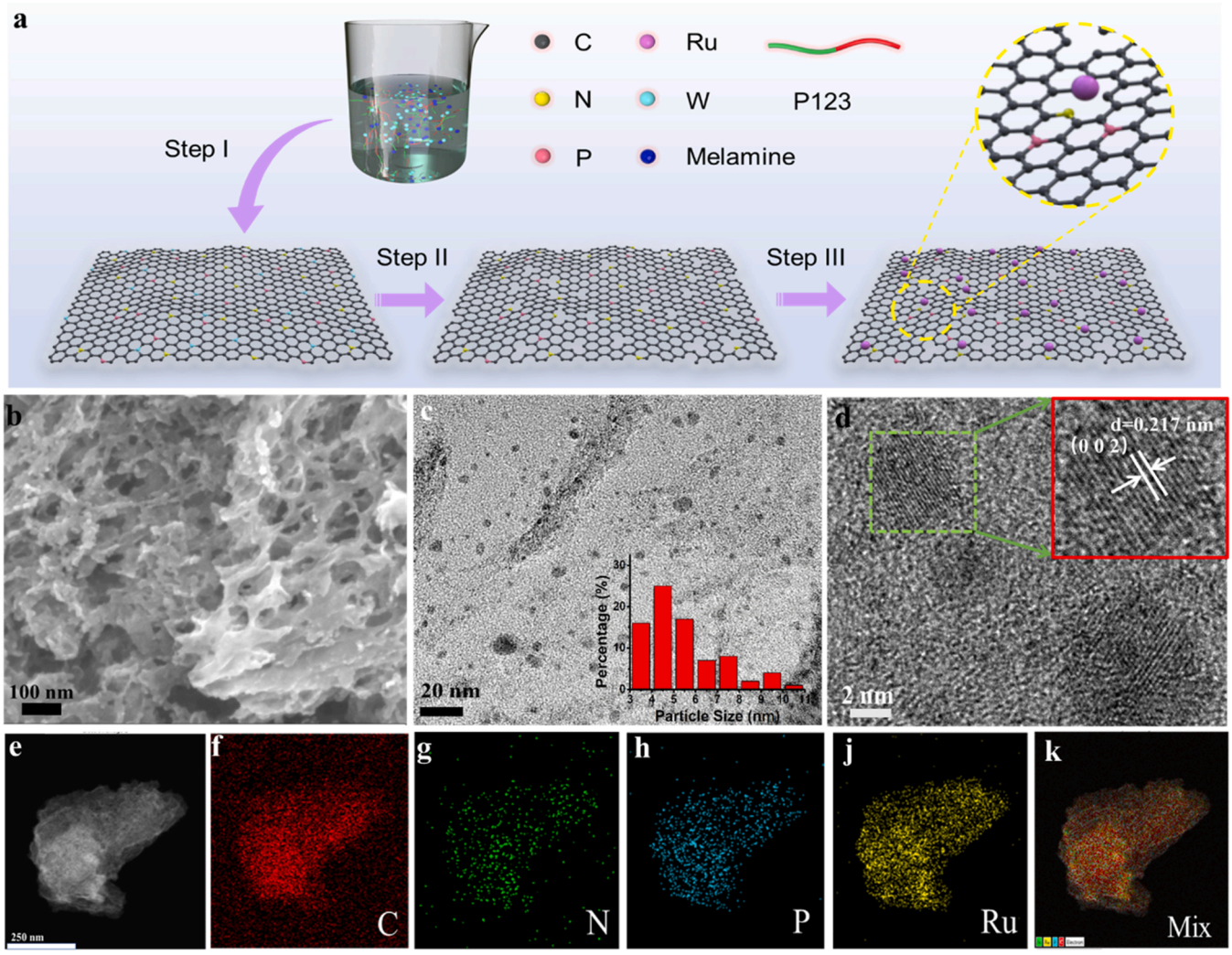

Fig. 1. (a) Schematic illustration of the synthesis of Ru nanoparticles on defect-rich N and P co-doped carbon nanosheets (Ru/D-NPC). (b) SEM images of Ru/D-NPC. (c) TEM image of Ru/D-NPC. The inset in (c) represents the size distribution of Ru NPs. (d) HRTEM images of Ru/D-NPC. The inset in (d) are the enlarged image taken from the square area marked. (e) High-angle annular dark field (HAADF) scanning transmission electron microscopy (STEM) and (f-k) HAADF-STEM energy-dispersive X-ray spectroscopy (EDS) elemental mapping of C (f), N (g), P(h), Ru(j) and mixture (k) elements in Ru/D-NPC.

obviously downshifted (Fig. 2b), while the N 1 s peaks upshift, compared to that of Ru/NPC, (Fig. S3b). It means that adjacent N atoms can transfer electrons to Ru, [15,32] proving that the strong electronic interaction between Ru and defective N-doped carbon nanosheets [19, 33,34]. The XPS results successfully confirm N and P dopants carbon significantly improve the surface properties of the substrate and modify the electronic state of Ru NPs, providing anchoring sites for the nucleation and growth of Ru. This electronic interaction between Ru and defective carbon is advantageous to reduce water dissociation barrier and improving HER performance [32,35].

Electron spin resonance (ESR) spectrum was further obtained to directly illustrate the defects in the Ru/NPC, Ru/D-NC, and Ru/D-NPC (Fig. 2e). Ru/D-NPC shows a much stronger vacancy defects-related ESR signal than Ru/NPC and Ru/D-NC, indicating that abundant defects are formed on the surface of Ru/D-NPC [36–39]. The inductively coupled plasma mass spectrometry (ICP-MS) displays the higher Ru content of ~9.9 wt% in Ru/D-NPC compared to Ru/D-NC (8.2 wt%) and Ru/NPC (3.9 wt%), suggesting the positive effect of defects on the anchoring of Ru species on the substrates. Raman spectrum was conducted to investigate the carbon matrix in the Ru/D-NPC. Two obvious strong peaks at 1354.20 cm^{-1} and 1594.74 cm^{-1} in Ru/D-NPC are assigned to typical D and G peaks of carbon (Fig. 2f). The I_D/I_G ratio of Ru/D-NPC is 0.89, smaller than that of D-NPC (1.01), indicates Ru coordinating with defective N in carbon, decreeing the degree of defective carbon. Compared to D-NPC (1358.51 cm^{-1}, 1600.16 cm^{-1}), the D peak and G peak of Ru/D-NPC show blue shifts, which can be attributed to chemically coordination of Ru nanoparticles with D-NPC [40,41].

3.2. Electrochemical evaluation for HER

The HER activity of Ru/D-NPC, Ru/NPC, Ru/D-NC, and Pt/C were initially conducted in 1 M KOH solution at 5 mV s^{-1} with iR-compensated. The electrochemical impedance spectroscopy (EIS) was measured to determine the compensated resistance (Figure. S4). HER polarization curves indicate the best HER performance of Ru/D-NPC (Figure. S5). Ultimately, the ECSA normalized HER polarization curves in Fig. 3a demonstrate that Ru/D-NPC holds better intrinsic electrocatalytic activity than Ru/NPC and Ru/D-NC. This is further confirmed by comparing the overpotentials at 10 mA cm^2 (η_{10}) and 30 mA cm^2 (η_{30}) (Fig. 3b). The η_{10} and η_{30} of Ru/D-NPC are 23 mV and 79 mV, respectively, outcompeting Ru/NPC (61,130 mV), Ru/D-NC (55, 111 mV) and Pt/C (45, 97 mV). And the mass activities of Ru/D-NPC, Ru/D-NC, Ru/NPC and 20 wt% Pt/C under the overpotential of 100 mV were also evaluated. As shown in Figure. S6, the highest mass activity (639.9 mA/mg_{Ru}) of Ru/D-NPC outperformes Ru/D-NC (395 mA/mg_{Ru}), Ru/NPC (326 mA/mg_{Ru}) and is almost two-fold of benchmarking Pt/C

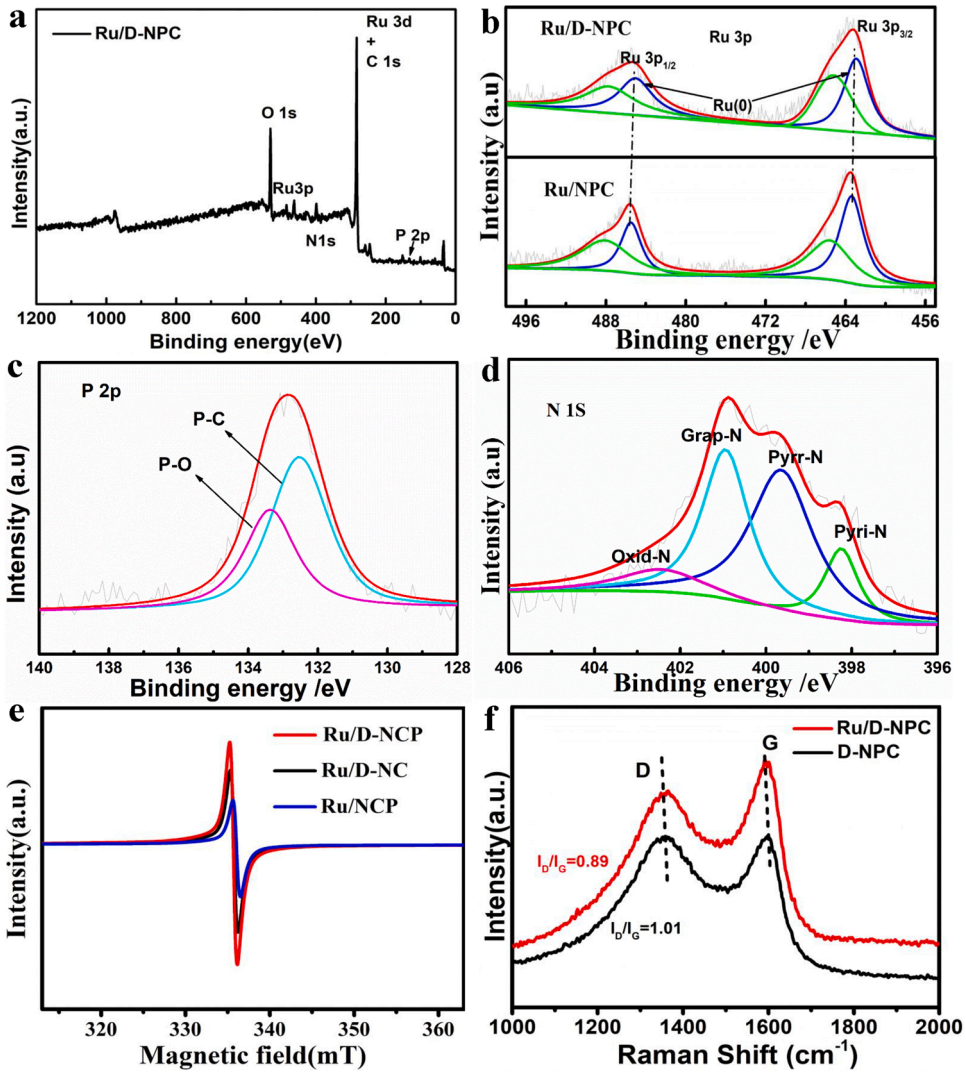

Fig. 2. (a) XPS full survey-scan of Ru/D-NPC, (b-d) High-resolution XPS spectra of Ru 3p, P 2p and N 1 s in Ru/D-NPC; respectively; (e) ESR spectra of Ru/D-NPC, Ru/NCP and Ru/D-NC. (f) Raman spectrum of Ru/D-NPC and D-NCP.

catalyst (320 mA/mg_{Pt}). The reaction kinetics during HER are evaluated by Tafel slopes (Fig. 3c). The Tafel value of Ru/D-NPC (38 mV dec^{-1}) is lower than Pt/C (51 mV dec^{-1}), Ru/D-NC (85.2 mV dec^{-1}) and Ru/NPC (109.7 mV dec^{-1}), manifesting that Ru/D-NPC exhibits fast H_2 generation kinetics than Ru/D-NC and Ru/NPC [41,42]. From Figure. S7, the exchange current densities (j_0) of Ru/D-NPC is 3.16 mA cm^{-2}, which is higher than those of Pt/C(1.41 mA cm^{-2}), Ru/NPC(3.01 mA cm^{-2}) and Ru/D-NC(2.51 mA cm^{-2}), manifesting that Ru/D-NPC holds best intrinsic catalytic activity. In addition, Ru/D-NPC exhibited a low charge transfer resistance (R_{ct}) of 30 Ω, which is much lower than those of Ru/NPC (63 Ω) and Ru/D-NC (57 Ω) (Fig. 3d), making clear that it owns a faster HER kinetics [39]. That is to say, the higher HER activity of the Ru/D-NPC electrode can be attributed to the smallest Tafel slope and minimal Rct.

Long-term durability is one key index to evaluate the excellence of electrocatalysts. The LSV curves show negligible decay after 3000 CV cycles (Fig. 3e). The chronopotentiometry curve of Ru/D-NPC was conducted under 20 mA cm^{-2} for 24 h. The real-time potential displays slight change, confirming the long-term durability of Ru/D-NPC for HER (Fig. 3f). The multicurrent chronopotentiometry response for Ru/D-NPC without iR compensation was also tested to furtherly evaluate the stability (Fig. S8). Notably, the overpotential increases step-by-step with the applied current density increased from 10 to 100 mA cm^{-2}. Even under the large current densities, the overpotentials still remains unchanged, demonstrating the robust stability of Ru/D-NPC electrode.

The HRTEM image of Ru/D-NPC after long-term HER in 1 M KOH shows that the average diameter of Ru nanoparticles is 5.6 nm without obvious morphology change. The comparison of XRD patterns gives the unchanged crystal structure of Ru (Fig S10a). The XPS spectra further illustrate that the composition of the Ru/D-NPC remains the same (Figure. S10b). These are attributed to the interaction between Ru and defective carbon that prevents the aggregation of Ru during the catalytic processes.

For further understanding the number of active sites and inherent activities of Ru/D-NPC in HER, the electrocatalytic active surface area (ECSA) was estimate by measuring double-layer capacitance (C_{dl}) [5,43,44]. As displayed in Figure. S11a–d, the C_{dl} of Ru/D-NPC is 26.4 mF cm^{-2}, which is close to 35.5 mF cm^2 calculated from EIS results (Fig. S12), and about 1.22-times and 1.52-times increasement compared to Ru/D-NC (21.6 mF cm^{-2}) and Ru/NPC (17.4 mF cm^{-2}), respectively. Such C_{dl} proves that Ru/D-NPC possesses a higher ECSA (440 cm^2) compared to Ru/D-NC (360 cm^2) and Ru/NPC (290 cm^2). Obviously, CV measurements reveal that our Ru/D-NPC has more active sites associated with the much increased HER performance relative to the controls. In addition, the intrinsic catalytic activity of Ru/D-NPC was also assessed by turnover frequency (TOF) [45]. The Ru/D-NPC catalysts shows

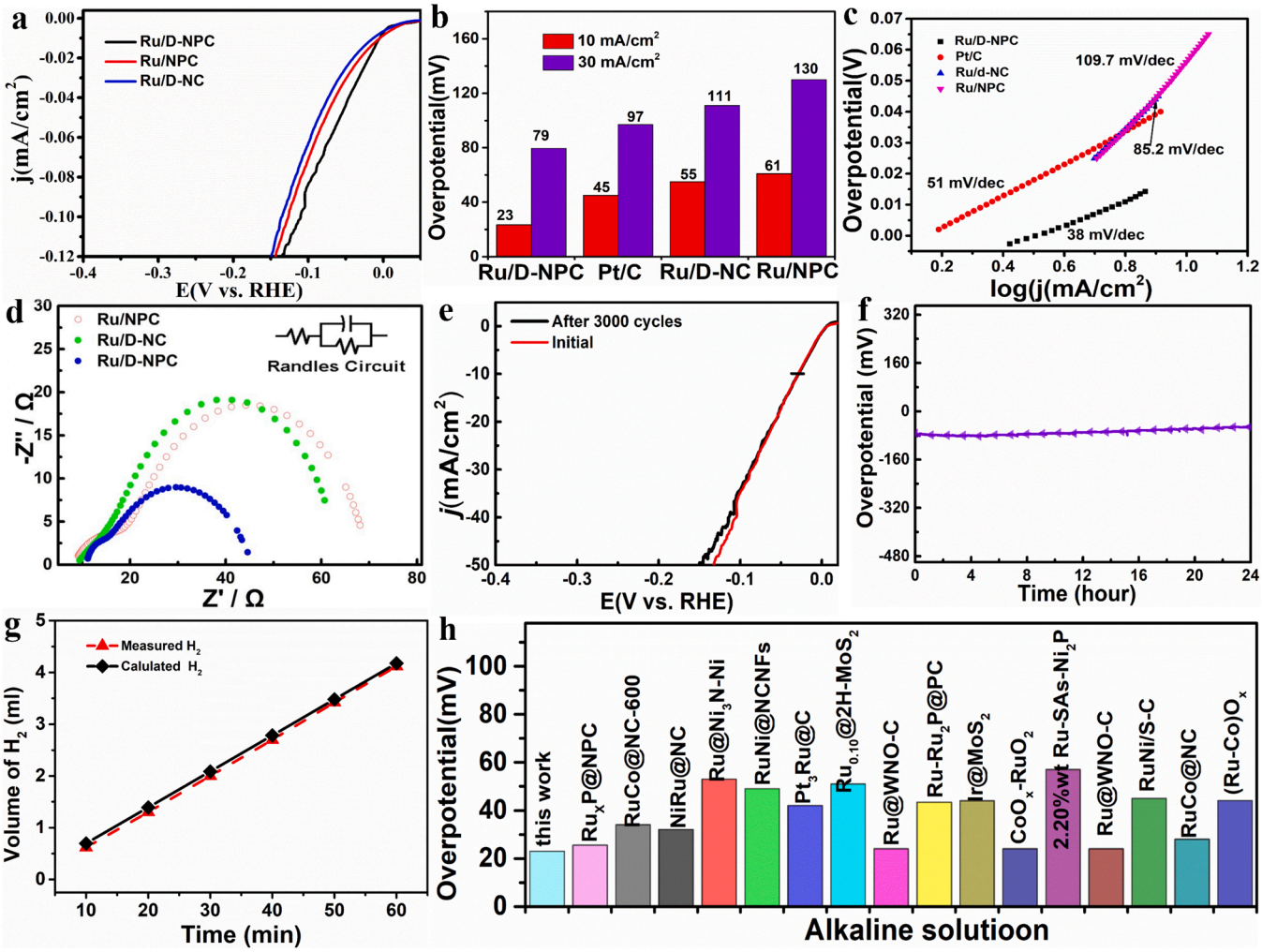

Fig. 3. (a) ECSA normalized HER polarization curves of the as-prepared Ru/D-NPC, Ru/NPC and Ru/D-NC electrocatalysts. (b) Corresponding overpotentials at j = 10 mA cm^{-2} and 30 mA cm^{-2}. (c) Corresponding Tafel plots. (d) Nyquist plots of Ru/NPC, Ru/D-NC and Ru/D-NPC measured at overpotential of 120 mV. (e) Polarization curves recorded initial and after 3000 CV cycles for Ru/D-NPC. (f) The potential–time response curve for Ru/D-NPC under 20 mA cm^{-2} for 24 h. (g) Experiment and theory amount of H_2 as a function of time. (h) HER activity comparison graph showing overpotentials at a current density of 10 mA cm^{-2} for Ru-based and precious-metal-based catalysts reported in alkaline solution.

significantly larger TOF values of 0.130 s^{-1} at an overpotential of 100 mV in alkaline, representing 1.33-fold and 1.18-fold increases compared to Ru/D-NC (0.098 s^{-1}) and Ru/NPC (0.110 s^{-1}). Besides, quantification of the evolved H_2 was measured by the water drainage method (Figure. S13). The amount of measured H_2 is very close to that of the theoretical value, representing a Faradaic efficiency of 95.4% on our Ru/D-NPC in alkaline media (Fig. 3g). The weight ratio of Ru in Ru/D-NPC-1 and Ru/D-NPC-3 is adjusted to optimize the HER performance. The η_{10} of Ru/D-NPC is 23 mV (Figure. S14), outperforming Ru/D-NPC-1 (51 mV) and Ru/D-NPC (28 mV). The mass activities of Ru/D-NPC under the overpotential of 100 mV is 639.9 mA/mg_{Ru}, outperforming Ru/D-NPC-1 (416 mA/mg_{Ru}) and Ru/D-NPC-3 (474 mA/mg_{Ru}), suggesting that Ru/D-NPC owns the highest mass activity. Importantly, the Ru/D-NPC also exhibits a high activity toward alkaline HER (η_{10} =23 mV), outperforms most reported noble-metal based electrocatalysts. (Fig. 3h and table S1).

The HER activity of Ru/D-NPC in neutral and acid solutions were also explored. As displayed in Fig. 4a and d, Ru/D-NPC electrocatalysts reveals outstanding HER activity in both 1.0 M PBS and 0.5 M H_2SO_4 solution, rendering low overpotentials of 61 and 68 mV at 10 mA cm^{-2}, respectively. The Ru/D-NPC catalysts shows significantly larger TOF values of 0.052 s^{-1} and 0.088 s^{-1} at overpotential of 100 mV in neutral and acid media, respectively, exceeding to Ru/D-NC (0.043 s^{-1},0.086 s^{-1}) and Ru/NPC (0.039 s^{-1},0.08 s^{-1}). The Tafel slope of Ru/D-NPC is 112.4 mV dec^{-1} and 41.7 mV dec^{-1} in pH = 7 and pH = 0 aqueous media, respectively, representing that the electrocatalyst adheres to the Volmer–Heyrovsky mechanism (Fig. 4b and e), suggesting electrochemical desorption process is the rate-determining step [46,47]. The Nyquist plots prove that the charge transfer impedance of Ru/D-NPC electrode is smallest among all the studied samples in acidic and neutral media, making clear that it owns a fastest HER kinetics (Figure. S15). In addition, Ru/D-NPC also poses better stability in both solutions (Fig. 4c and f). Analyzing the XPS data and TEM after long-term HER process, Ru/D-NPC is indeed a stable electrocatalyst toward HER in 0.5 M H_2SO_4 and 1 M PBS (Figure. S16-S17). In order to highlight the difference in catalytic activity of Ru/D-NPC compared with the reported Ru-based catalysts, the η10 value as a criterion toward HER in neutral and acid solutions are summarized (Fig. 4g, Table S2–S3). Noting, our Ru/D-NPC catalysts are able to effectively improve the HER activity. Overall, these results clearly indicate that Ru/D-NPC poses a highly catalytic activity toward HER over the entire pH range (pH 0–14), showing a competitive performance [48]. Ru/D-NPC and IrO_2 were used as cathode and anode catalyst to assemble an alkaline electrolyzer in 1 M KOH (Fig. 4h). It shows a low full-cell voltage of 1.57 V at 10 mA cm^{-2} compared to the Pt/C||IrO_2 (1.62 V at 10 mA cm^{-2}). Moreover, Ru/D-NPC ||IrO_2 couple displays a low full-cell voltage,

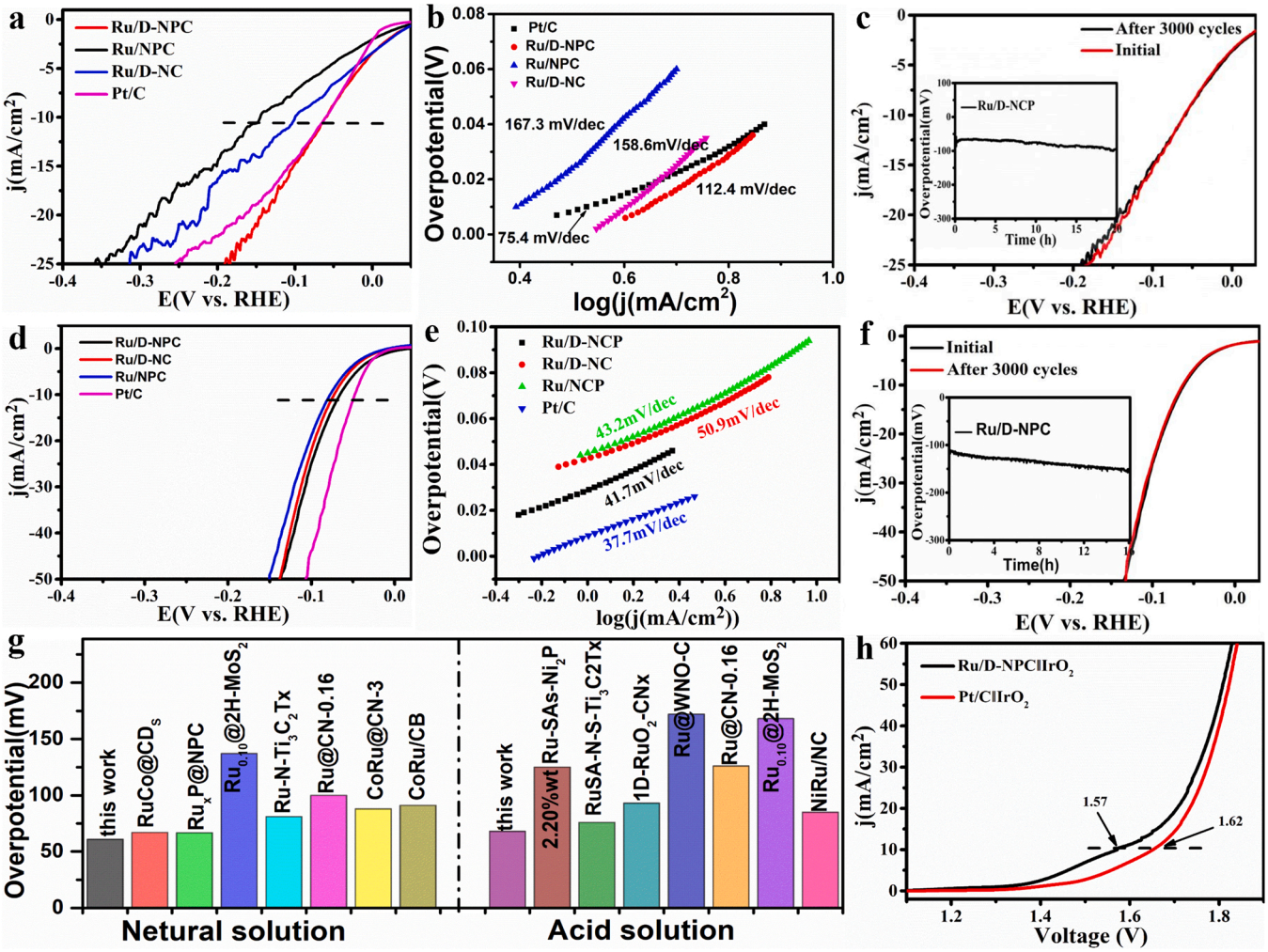

Fig. 4. Polarization curves of Pt/C, Ru/D-NPC, Ru/D-NC, and Ru/NPC in 1 M PBS (a) and in 0.5 M H_2SO_4 (d). Corresponding Tafel plots(b) and (e). Polarization curves of Ru/D-NPC before and after 3000 CV cycles in 1 M PBS (c) and 0.5 M H_2SO_4 (F) (inset: The potential–time response curve of the Ru/D-NPC under 20 mA cm^{-2} in 0.5 M H_2SO_4 or 1 M PBS without iR correction). (g) HER activity comparison graph showing overpotentials at a current density of 10 mA cm^{-2} for Ru-based and Precious-metal-based catalysts reported in neutral and acid solution. (h) Polarization curves without iR-compensation of Ru/D-NPC|| IrO_2, Pt/C toward overall water splitting in 1 M KOH recorded at 5 mV s^{-1}.

exceeding those of commercial Pt/C||IrO_2 in 0.5 M H_2SO_4 and 1 M PBS (Figure. S18). The Ru/D-NPC ||IrO_2 also exhibits the reasonable electrochemical stability (Figure. S19), suggest the application potential.

3.3. Theoretical calculations

DFT calculations were performed to fundamentally comprehend into the excellent HER activity of Ru/D-NPC. Ru cluster on the bridge of N and P in defect carbon is used as an initial structure (Fig. 5a). A further calculation configuration optimizes the anchor sites of Ru clusters and indicates the top sites of defect N toms is the optimum (Fig. 5b). Based on the electron localization function analysis map (Fig. 5c), defects N as electron donor, transfer electrons to Ru, causing defective N with positive charge while the Ru with a partial negative charge, promoting break the H–OH bond, thereby facilitating the HER performance [45,49]. DFT calculations suggests the absence of Ru-P bond. The above results confirm Ru cluster is more easily adsorbed around the defective N site compared to the P site.

The partial electronic density of states (PDOS) of Ru, N in Ru/D-NPC indicate that their S and P orbitals are partially overlapping with each other, indicating an interaction between N and Ru. These will promote the formation of metal-N bonds (Fig. S20). In this process, D-NPC provides the N coordination sites for nucleation of Ru, as well as strong affinity between Ru and carbon, promoting the uniform distribution of Ru clusters on carbon sheets, limiting aggregation of metal atoms during high-temperature catalysis.

The HER activity is strongly relied on the Gibbs free energy of hydrogen adsorption (ΔG_H) on the catalysts surface (Figure. S21). The ΔG_H values on various catalysts (Fig. 5d) indicate a much smaller ΔG_H value of Ru/D-NPC compared to Ru/NPC, Ru/NC, Ru/C and Pt(111) catalysts. Ru/D-NPC owns appropriate hydrogen chemisorption and releasing ability, thereby exhibiting a super HER activity. That is to say, after introducing phosphorus and defect N, the collaborative effect between N-P doped C and Ru in Ru/D-NPC significantly decreases the proton adsorption energy on Ru/C, thereby facilitating the surface hydrogen generation, also explaining why Ru/D-NPC displays outstanding HER activity.

Compared to Ru/C, Ru/NPC, the D-band centers (ε_d) of Ru d orbital in Ru/D-NPC moves to low energy level (Fig. 5E), meaning a weakened interaction between adsorbed oxygen species and Ru site, accordingly favoring the HER performance. In general, the Ru/D-NPC nanocatalyst can be built to adjust the electronic structure of noble metal Ru by metal-support interactions, optimizes the adsorption energy of intermediates in HER key steps, beneficial to the water splitting process.

Based on the above experimental and analytic results, the excellent activities of the Ru/D-NPC materials toward HER in a wide pH range are

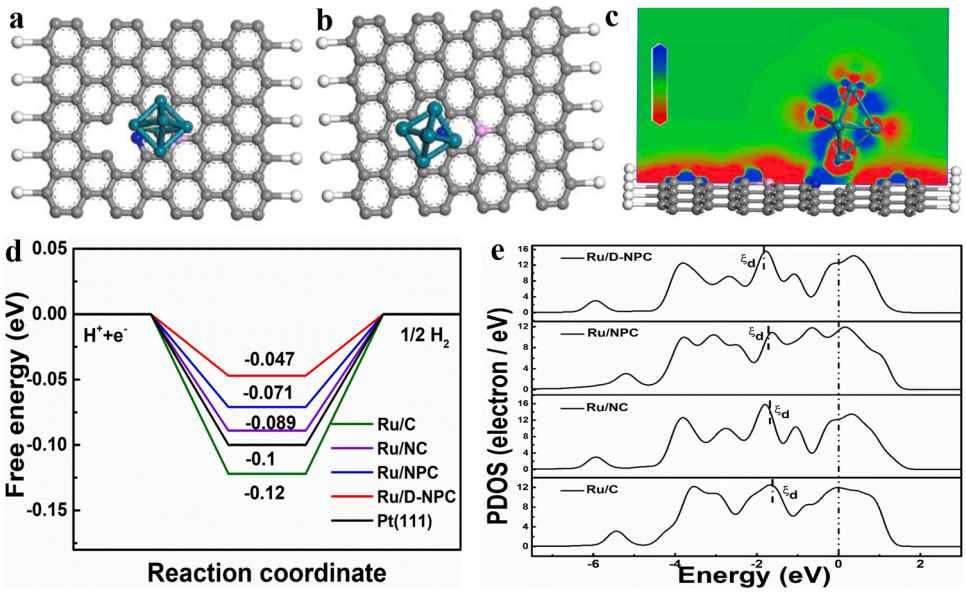

Fig. 5. (a-b) Atomic structures of Ru/D-NPC before and after optimizing the calculation configuration. (c) The electron localization function analysis mapped for the first atomic layer in Ru/D-NPC. (d) ΔG_H profiles for the HER on Ru/D-NPC, Ru/C, Ru/NC, Ru/NPC and Pt(111), (e) The partial electronic density of Ru states and D-band center for Ru/D-NPC, Ru/C, Ru/NC, and Ru/NPC.

attributed to the following aspects: (i) Ru nanoparticle uniformly distributing on the entire supports, improving the Ru utilization [15], (ii) Extensive defectives occur in the supports of Ru/D-NPC, improving the conductivity, conductive to the HER activity [50], (iii) N and P dopants significantly improve the surface properties of the substrate and modulate the electronic state of Ru NP, thereby enhancing the electrocatalytic performance for the HER [35,51]. (IV) Ru nanoparticles confined with C inhibit the aggregation during the catalytic processes, enhancing the durability of catalytic [52].

4. Conclusion

In conclusion, we found that interfacial binding of Ru nanocatalysts with defect-rich nitrogen and phosphorus co-doped carbon (Ru/D-NPC) boosted the intrinsic HER kinetics on the active Ru sites. A combined study of experimental observations with DFT calculations have confirmed that N and P dopants in carbon lowers the d band orbits of Ru due to strong electron interaction originating from their chemical bonding. The Ru/D-NPC catalysts therefore exhibit a record HER activity at all pH values. In particular, it shows a low overpotential of 23 mV at 10 mA cm^{-2} in alkaline, outperforming the previously reported performance cap and the commercial Pt/C catalysts. Our results provide a key understanding of HER mechanism on supporting nanocatalyst systems and a synthesis methodology for interfacially bonding of active nanocatalysts with selected proper substrates.

CRediT authorship contribution statement

Wenqiang Li: Investigation, Writing – original draft, Funding acquisition. **Heng Zhang:** Methodology. **Ka Zhang:** Investigation. **Wenxuan Hu:** Investigation. **Zezhong Cheng:** Methodology. **Haipeng Chen:** Methodology. **Xun Feng:** Investigation, Visualization, Writing – review & editing. **Tao Peng:** Writing – review & editing. **Zongkui Kou:** Investigation, Writing – review & editing, Supervision.

Declaration of Competing Interest

The authors declare no conflict of interest.

Acknowledgments

This work was supported by the Natural Science Foundation of China (Nos. 21671114, 22008098, and U1804131), and the Tackle Key Problem of Science and Technology Project of Henan Province, China (No. 202102210245), and Program for Science and Technology Innovation Talents in Universities of Henan Province (No. 21IRTSTHN004), Natural Science Foundation of Henan Province (No. 202300410288).

Appendix A. Supporting information

Supplementary data associated with this article can be found in the online version at doi:10.1016/j.apcatb.2022.121095.

References

[1] T. Hisatomi, J. Kubota, K. Domen, Recent advances in semiconductors for photocatalytic and photoelectrochemical water splitting, Chem. Soc. Rev. 43 (2014) 7520–7535.
[2] M.D. Symes, L. Cronin, Decoupling hydrogen and oxygen evolution during electrolytic water splitting using an electron-coupled-proton buffer, Nat. Chem. 5 (2013) 403–409.
[3] D. Chen, R.H. Lu, Z.H. Pu, J.W. Zhu, H.W. Li, F. Liu, S. Hu, X. Luo, J.S. Wu, Y. Zhao, S.C. Mu, Ru-doped 3D flower-like bimetallic phosphide with a climbing effect on overall water splitting, Appl. Catal. B Environ. 279 (2020), 119396.
[4] T. Wang, P. Wang, W. Zang, X. Li, D. Chen, Z. Kou, S. Mu, J. Wang, Nanoframes of Co_3O_4-Mo_2N heterointerfaces enable high-performance bifunctionality towards both electrocatalytic HER and OER, Adv. Funct. Mater. (2021), 2107382, https://doi.org/10.1002/adfm.202107382.
[5] P. Wang, T. Wang, R. Qin, Z. Pu, C. Zhang, J. Zhu, D. Chen, D. Feng, Z. Kou, S. Mu, J. Wang, Swapping catalytic active sites from cationic Ni to anionic S in nickel sulfide enables more efficient alkaline hydrogen generation, Adv. Energy Mater. (2021), https://doi.org/10.1002/aenm.202103359.
[6] I. Roger, M.A. Shipman, M.D. Symes, Earth-abundant catalysts for electrochemical and photoelectrochemical water splitting, Nat. Rev. Chem. 1 (2017) 13.
[7] J.Q. Shan, T. Ling, K. Davey, Y. Zheng, S.Z. Qiao, Transition-metal-doped RuIr bifunctional nanocrystals for overall water splitting in acidic environments, Adv. Mater. 31 (2019), 1900510.
[8] Y. Zheng, Y. Jiao, Y.H. Zhu, L.H. Li, Y. Han, Y. Chen, M. Jaroniec, S.Z. Qiao, High electrocatalytic hydrogen evolution activity of an anomalous ruthenium catalyst, J. Am. Chem. Soc. 138 (2016) 16174–16181.
[9] S. Yuan, Z.H. Pu, H. Zhou, J. Yu, I.S. Amiinu, J.W. Zhu, Q.R. Liang, J.L. Yang, D. P. He, Z.Y. Hu, G. Van Tendeloo, S.C. Mu, A universal synthesis strategy for single atom dispersed cobalt/metal clusters heterostructure boosting hydrogen evolution catalysis at all pH values, Nano Energy 59 (2019) 472–480.

[10] C.H. Chen, D.Y. Wu, Z. Li, R. Zhang, C.G. Kuai, X.R. Zhao, C.K. Dong, S.Z. Qiao, H. Liu, X.W. Du, Ruthenium-based single-atom alloy with high electrocatalytic activity for hydrogen evolution, Adv. Energy Mater. 9 (2019), 1803913.
[11] H.X. Wang, M. Zhou, X.J. Bo, L.P. Guo, Rapid and facile laser-assistant preparation of Ru-ZIF-67-derived CoRu nanoalloy@N-doped graphene for electrocatalytic hydrogen evolution reaction at all pH values, Electrochim. Acta 382 (2021), 138337.
[12] Q. He, D. Tian, H. Jiang, D. Cao, S. Wei, D. Liu, P. Song, Y. Lin, L. Song, Achieving efficient alkaline hydrogen evolution reaction over a Ni5P4 catalyst incorporating single-atomic Ru sites, Adv. Mater. 32 (2020), 1906972.
[13] Z. Wei, Z. Zhao, J. Wang, Q. Zhou, C. Zhao, Z. Yao, J. Wang, Oxygen-deficient TiO 2 and carbon coupling synergistically boost the activity of Ru nanoparticles for the alkaline hydrogen evolution reaction, J. Mater. Chem. A 9 (2021) 10160–10168.
[14] W. Li, B. Feng, L. Yi, J. Li, W. Hu, Highly efficient alkaline water splitting with Ru-doped Co−V layered double hydroxide nanosheets as a bifunctional electrocatalyst, ChemSusChem 14 (2021) 730–737.
[15] X. Sun, X. Gao, J. Chen, X. Wang, H. Chang, B. Li, D. Song, J. Li, H. Li, N. Wang, Ultrasmall Ru nanoparticles highly dispersed on sulfur-doped graphene for HER with high electrocatalytic performance, ACS Appl. Mater. Interfaces 12 (2020) 48591–48597.
[16] Y. Lee, J.H. Ahn, S. Shin, S.-H. Jung, H.-S. Park, Y.-G. Cho, D.-G. Lee, H. Kong, J. H. Lee, H.-K. Song, Metal-nitrogen intimacy of the nitrogen-doped ruthenium oxide for facilitating electrochemical hydrogen production, Appl. Catal. B Environ. 303 (2022), 120873.
[17] L. Fang, Y. Wang, X. Yang, H. Zhang, Y. Wang, Uniform OsP2 nanoparticles anchored on N,P-doped carbon: a new electrocatalyst with enhanced activity for hydrogen generation at all pH values, J. Catal. 370 (2019) 404–411.
[18] G.-f Long, K. Wan, M.-y Liu, Z.-x Liang, J.-h Piao, P. Tsiakaras, Active sites and mechanism on nitrogen-doped carbon catalyst for hydrogen evolution reaction, J. Catal. 348 (2017) 151–159.
[19] Z. Liu, X. Yang, G. Hu, L. Feng, Ru nanoclusters coupled on Co/N-doped carbon nanotubes efficiently catalyzed the hydrogen evolution reaction, ACS Sustain. Chem. Eng. 8 (2020) 9136–9144.
[20] F. Zhou, R. Sa, X. Zhang, S. Zhang, Z. Wen, R. Wang, Robust ruthenium diphosphide nanoparticles for pH-universal hydrogen evolution reaction with platinum-like activity, Appl. Catal. B Environ. 274 (2020), 119092.
[21] D.N. Sangeetha, M. Selvakumar, Active-defective activated carbon/MoS2 composites for supercapacitor and hydrogen evolution reactions, Appl. Surf. Sci. 453 (2018) 132–140.
[22] G. Meng, H. Tian, L.X. Peng, Z.H. Ma, Y.F. Chen, C. Chen, Z.W. Chang, X.Z. Cui, J. L. Shi, Ru to W electron donation for boosted HER from acidic to alkaline on Ru/WNO sponges, Nano Energy 80 (2021), 105531.
[23] X. Bai, Q.-Q. Pang, X. Du, S.-S. Yi, S. Zhang, J. Qian, X.-Z. Yue, Z.-Y. Liu, Integrating RuNi alloy in S-doped defective carbon for efficient hydrogen evolution in both acidic and alkaline media, Chem. Eng. J. 417 (2021), 129319.
[24] V.H. Hoa, D.T. Tran, H.T. Le, N.H. Kim, J.H. Lee, Hierarchically porous nickel cobalt phosphide nanoneedle arrays loaded micro-carbon spheres as an advanced electrocatalyst for overall water splitting application, Appl. Catal. B Environ. 253 (2019) 235–245.
[25] X.H. Xia, Y.D. Wang, D.H. Wang, Y.Q. Zhang, Z.X. Fan, J.P. Tu, H. Zhang, H.J. Fan, Atomic-layer-deposited iron oxide on arrays of metal/carbon spheres and their application for electrocatalysis, Nano Energy 20 (2016) 244–253.
[26] Y.L. Wu, X.F. Li, Y.S. Wei, Z.M. Fu, W.B. Wei, X.T. Wu, Q.L. Zhu, Q. Xu, Ordered macroporous superstructure of nitrogen-doped nanoporous carbon implanted with ultrafine Ru nanoclusters for efficient pH-universal hydrogen evolution reaction, Adv. Mater. 33 (2021), 2006965.
[27] Y.Z. Li, J. Abbott, Y.C. Sun, J.M. Sun, Y.C. Du, X.J. Han, G. Wu, P. Xu, Ru nanoassembly catalysts for hydrogen evolution and oxidation reactions in electrolytes at various pH values, Appl. Catal. B Environ. 258 (2019), 117952.
[28] J.L. Liu, Y. Zheng, D.D. Zhu, A. Vasileff, T. Ling, S.Z. Qiao, Identification of pH-dependent synergy on Ru/MoS2 interface: a comparison of alkaline and acidic hydrogen evolution, Nanoscale 9 (2017) 16616–16621.
[29] C.D. Wagner, L.H. Gale, R.H. Raymond, Two-dimensional chemical state plots: a standardized data set for use in identifying chemical states by x-ray photoelectron spectroscopy, Anal. Chem. 51 (1979) 466–482.
[30] J. Wang, Z.Z. Wei, S.J. Mao, H.R. Li, Y. Wang, Highly uniform Ru nanoparticles over N-doped carbon: pH and temperature-universal hydrogen release from water reduction, Energy Environ. Sci. 11 (2018) 800–806.
[31] S. Yang, J.-Y. Zhu, X.-N. Chen, M.-J. Huang, S.-H. Cai, J.-Y. Han, J.-S. Li, Self-supported bimetallic phosphides with artificial heterointerfaces for enhanced electrochemical water splitting, Appl. Catal. B Environ. 304 (2022), 120914.
[32] L.X. Guo, J.Y. Wang, X. Teng, Y.Y. Liu, X.M. He, Z.F. Chen, A. Novel, Bimetallic nickel-molybdenum carbide nanowire array for efficient hydrogen evolution, ChemSusChem 11 (2018) 2717–2723.
[33] G.B. Chen, T. Wang, J. Zhang, P. Liu, H.J. Sun, X.D. Zhuang, M.W. Chen, X.L. Feng, Accelerated hydrogen evolution kinetics on NiFe-layered double hydroxide electrocatalysts by tailoring water dissociation active sites, Adv. Mater. 30 (2018), 1706279.
[34] Y.J. Wang, J.K. Wang, T.P. Xie, Q.Y. Zhu, D. Zeng, R. Li, X.D. Zhang, S.L. Liu, Ru doping in Ni(OH)(2) to accelerate water reduction kinetics for efficient hydrogen evolution reaction, Appl. Surf. Sci. 485 (2019) 506–512.
[35] C. Wang, F. Hu, H. Yang, Y. Zhang, H. Lu, Q. Wang, 1.82 wt% Pt/N, P co-doped carbon overwhelms 20 wt% Pt/C as a high-efficiency electrocatalyst for hydrogen evolution reaction, Nano Res. 10 (2016) 238–246.
[36] J. Yin, Y.X. Li, F. Lv, M. Lu, K. Sun, W. Wang, L. Wang, F.Y. Cheng, Y.F. Li, P.X. Xi, S.J. Guo, Oxygen vacancies dominated NiS2/CoS2 interface porous nanowires for portable Zn-Air batteries driven water splitting devices, Adv. Mater. 29 (2017), 1704681.
[37] F.C. Lei, Y.F. Sun, K.T. Liu, S. Gao, L. Liang, B.C. Pan, Y. Xie, Oxygen vacancies confined in ultrathin indium oxide porous sheets for promoted visible-light water splitting, J. Am. Chem. Soc. 136 (2014) 6826–6829.
[38] S. Mohajernia, S. Hejazi, A. Mazare, N.T. Nguyen, I. Hwang, S. Kment, G. Zoppellaro, O. Tomanec, R. Zboril, P. Schmuki, Semimetallic core-shell TiO2 nanotubes as a high conductivity scaffold and use in efficient 3D-RuO2 supercapacitors, Mater. Today Energy 6 (2017) 46–52.
[39] Z.Z. Wei, Z.J. Zhao, J. Wang, Q. Zhou, C.X. Zhao, Z.H. Yao, J.G. Wang, Oxygen-deficient TiO2 and carbon coupling synergistically boost the activity of Ru nanoparticles for the alkaline hydrogen evolution reaction, J. Mater. Chem. A 9 (2021) 10160–10168.
[40] G. Li, K. Zheng, W. Li, Y. He, C. Xu, Ultralow Ru-induced bimetal electrocatalysts with a Ru-enriched and mixed-valence surface anchored on a hollow carbon matrix for oxygen reduction and water splitting, ACS Appl. Mater. Interfaces 12 (2020) 51437–51447.
[41] B. Sarkar, D. Das, K.K. Nanda, pH-dependent hydrogen evolution using spatially confined ruthenium on hollow N-doped carbon nanocages as a Mott–Schottky catalyst, J. Mater. Chem. A 9 (2021) 13958–13966.
[42] B.G. Mao, P.P. Sun, Y. Jiang, T. Meng, D.L. Guo, J.W. Qin, M.H. Cao, Identifying the transfer kinetics of adsorbed hydroxyl as a descriptor of alkaline hydrogen evolution reaction, Angew. Chem. Int. Ed. 59 (2020) 15232–15237.
[43] F. Luo, H. Hu, X. Zhao, Z. Yang, Q. Zhang, J. Xu, T. Kaneko, Y. Yoshida, C. Zhu, W. Cai, Robust and stable acidic overall water splitting on Ir single atoms, Nano Lett. 20 (2020) 2120–2128.
[44] J.-S. Li, M.-J. Huang, Y.-W. Zhou, X.-N. Chen, S. Yang, J.-Y. Zhu, G.-D. Liu, L.-J. Ma, S.-H. Cai, J.-Y. Han, RuP2-based hybrids derived from MOFs: highly efficient pH-universal electrocatalysts for the hydrogen evolution reaction, J. Mater. Chem. A 9 (2021) 12276–12282.
[45] A. Salah, H.-D. Ren, N. Al-Ansi, F.-Y. Yu, Z.-L. Lang, H. Tan, Y.-G. Li, Ru/Mo2C@NC Schottky junction-loaded hollow nanospheres as an efficient hydrogen evolution electrocatalyst, J. Mater. Chem. A 9 (2021) 20518–20529.
[46] L.N. Zhang, S.H. Li, H.Q. Tan, S.U. Khan, Y.Y. Ma, H.Y. Zang, Y.H. Wang, Y.G. Li, MoP/Mo2C@C: a new combination of electrocatalysts for highly efficient hydrogen evolution over the entire pH range, ACS Appl. Mater. Interfaces 9 (2017) 16270–16279.
[47] F. Luo, Q. Zhang, X.X. Yu, S.L. Xiao, Y. Ling, H. Hu, L. Guo, Z.H. Yang, L. Huang, W. W. Cai, H.S. Cheng, Palladium phosphide as a stable and efficient electrocatalyst for overall water splitting, Angew. Chem. Int. Ed. 57 (2018) 14862–14867.
[48] Z.H. Pu, X. Ya, I.S. Amiinu, Z.K. Tu, X.B. Liu, W.Q. Li, S.C. Mu, Ultrasmall tungsten phosphide nanoparticles embedded in nitrogen-doped carbon as a highly active and stable hydrogen-evolution electrocatalyst, J. Mater. Chem. A 4 (2016) 15327–15332.
[49] Z.H. Pu, J.H. Zhao, I.S. Amiinu, W.Q. Li, M. Wang, D.P. He, S.C. Mu, A universal synthesis strategy for P-rich noble metal diphosphide-based electrocatalysts for the hydrogen evolution reaction, Energy Environ. Sci. 12 (2019) 952–957.
[50] Q. Qin, H. Jang, L. Chen, G. Nam, X. Liu, J. Cho, Low loading of RhxP and RuP on N, P codoped carbon as two trifunctional electrocatalysts for the oxygen and hydrogen electrode reactions, Adv. Energy Mater. 8 (2018), 1801478.
[51] Y. Pei, W. He, M. Wang, J. Wang, T. Sun, L. Hu, J. Zhu, Y. Tan, J. Wang, RuCo alloy trifunctional electrocatalysts with ratio-dependent activity for Zn-air batteries and self-powered water splitting, Chem. Commun. 57 (2021) 1498–1501.
[52] C. Gao, J. Wang, H.X. Xu, Y.J. Xiong, Coordination chemistry in the design of heterogeneous photocatalysts, Chem. Soc. Rev. 46 (2017) 2799–2823.